Published in final edited form as:
Sci Transl Med. 2014 June 11; 6(240): 240ra75. doi:10.1126/scitranslmed.3007646.

Alkylphosphocholine Analogs for Broad-Spectrum Cancer Imaging and Therapy

Jamey P. Weichert[1,2,3,4,*], **Paul A. Clark**[5], **Irawati K. Kandela**[4], **Abram M. Vaccaro**[4], **William Clarke**[4], **Marc A. Longino**[1,4], **Anatoly N. Pinchuk**[1,4], **Mohammed Farhoud**[3], **Kyle I. Swanson**[5], **John M. Floberg**[2], **Joseph Grudzinski**[2,4], **Benjamin Titz**[4], **Anne M. Traynor**[6], **Hong-En Chen**[5], **Lance T. Hall**[1], **Christopher J. Pazoles**[4], **Perry J. Pickhardt**[1], and **John S. Kuo**[3,5,*]

[1]Department of Radiology, University of Wisconsin School of Medicine and Public Health, Madison, WI 53792, USA.

[2]Department of Medical Physics, University of Wisconsin School of Medicine and Public Health, Madison, WI 53792, USA.

[3]Carbone Cancer Center, University of Wisconsin School of Medicine and Public Health, Madison, WI 53792, USA.

[*]Corresponding author. jweichert@uwhealth.org (J.P.W.); j.kuo@neurosurgery.wisc.edu (J.S.K.).

SUPPLEMENTARY MATERIALS

www.sciencetranslationalmedicine.org/cgi/content/full/6/240/240ra75/DC1

Materials and Methods
Fig. S1. Preferential cancer cell uptake of CLR1501.
Fig. S2. Preferential ^{125}I-CLR1404 uptake and retention in cancer cells in vitro.
Fig. S3. Uptake and retention of ^{125}I-CLR1404 after lipid raft disruption in prostate carcinoma cells.
Fig. S4: Flow cytometry analysis of CLR1501 GSC labeling.
Fig. S5. In vivo time course of biodistribution and tumor uptake of ^{124}I-CLR1404 and ^{18}F-FDG in a prostate tumor model.
Fig. S6. Dual modality PET/CT virtual colonoscopy in rodents.
Fig. S7. Tumor growth and animal survival after ^{131}I-CLR1404 therapy.
Fig. S8. Recurrent World Health Organization grade III astrocytoma.
Fig. S9. ^{131}I-CLR1404 SPECT/CT imaging of metastatic colorectal cancer.
Fig. S10. Synthesis of optical APC analogs.
Table S1. ^{124}I-CLR1404 uptake in tumor xenografts.
Table S2. Patient information.
Movie S1. Cellular uptake of CLR1501 in prostate cancer cells.
Movie S2. Dual modality PET/CT virtual colonoscopy in the Pirc rat model. References (37–40)

Author contributions: A.M.V. designed and carried out the biological assays. I.K.K. designed and conducted the biological assays and confocal microscopic imaging. P.A.C. designed and conducted all biological assays related to cancer stem cells, interpreted data, and cowrote and edited the manuscript. K.I.S. and H.-E.C. conducted experiments with cancer stem cells and xenografts. W.C. helped design biological assays. M.A.L. formulated all agents for in vivo injection. A.N.P. synthesized and analyzed all APC analogs. J.G. and M.F. performed preclinical in vivo PET/CT imaging and quantification studies. J.G. and B.T. performed clinical image analysis and quantification. P.J.P. analyzed clinical images and helped edit the manuscript. J.M.F. carried out preclinical PET image acquisition, reconstruction, and quantification. A.M.T. and L.T.H. recruited patients for imaging studies and interpreted all clinical PET/CT images. C.J.P. interpreted data and cowrote and edited the manuscript. J.S.K. recruited patients for imaging studies, designed experiments, interpreted the data, provided administrative support, and cowrote and edited the manuscript. J.P.W. carried out radioiodination procedures, designed experiments, interpreted the preclinical data, provided administrative support, and cowrote and edited the manuscript.

Competing interests: J.P.W. and M.A.L. are cofounders of Cellectar Biosciences Inc., which owns licensing and patent rights to CLR1404 and related compounds described in this paper. P.J.P. and authors associated with Cellectar Biosciences Inc. were employees of and/or shareholders in Cellectar Biosciences Inc. All other authors declare that they have no competing interests.

Data and materials availability: CLR analogs and GSC lines can be requested via materials transfer agreements from Cellectar Biosciences or the University of Wisconsin-Madison, respectively.

[4]Cellectar Biosciences Inc., 3301 Agriculture Drive, Madison, WI 53716, USA.

[5]Department of Neurological Surgery, University of Wisconsin School of Medicine and Public Health, Madison, WI 53792, USA.

[6]Department of Medicine, University of Wisconsin School of Medicine and Public Health, Madison, WI 53792, USA.

Abstract

Many solid tumors contain an overabundance of phospholipid ethers relative to normal cells. Capitalizing on this difference, we created cancer-targeted alkylphosphocholine (APC) analogs through structure-activity analyses. Depending on the iodine isotope used, radioiodinated APC analog CLR1404 was used as either a positron emission tomography (PET) imaging (^{124}I) or molecular radiotherapeutic (^{131}I) agent. CLR1404 analogs displayed prolonged tumor-selective retention in 55 in vivo rodent and human cancer and cancer stem cell models. ^{131}I-CLR1404 also displayed efficacy (tumor growth suppression and survival extension) in a wide range of human tumor xenograft models. Human PET/CT (computed tomography) and SPECT (single-photon emission computed tomography)/CT imaging in advanced-cancer patients with ^{124}I-CLR1404 or ^{131}I-CLR1404, respectively, demonstrated selective uptake and prolonged retention in both primary and metastatic malignant tumors. Combined application of these chemically identical APC-based radioisosteres will enable personalized dual modality cancer therapy of using molecular ^{124}I-CLR1404 tumor imaging for planning ^{131}I-CLR1404 therapy.

INTRODUCTION

Selective delivery of diagnostic imaging and therapy agents to malignant tumors while sparing healthy tissues continues to be the major goal in cancer research and in clinical practice. Approaches to achieve this goal are reflected in therapeutic agents that are already approved or in development. Tumor-targeting vehicles based on antibodies, viruses, peptides, and nanoparticles have been used to deliver a wide range of “payloads” to cancer cells, including radioactive isotopes, imaging agents, oncolytic viruses, metals, and chemotherapeutic drugs (1–8). Currently available cancer therapy modalities offer either broad applicability across cancer types (for example, external beam radiation, surgery, cytotoxic drugs) or cancer selectivity based on higher expression of drug targets (genes) in cancer cell subpopulations compared to normal cells (for example, *PML-RAR*α, *BCR-ABL*, *c-kit*, *EGFR*, *ERBB*2/*Her*2/*neu*). Still, many cancers recur despite the initial disease control and therapeutic efficacy of many available cancer therapies. Recent evidence suggests that cancer recurrence likely involves failure to eradicate cancer cells that are relatively resistant to current therapies, such as cancer stem cells (or cancer stem-like cells) (9–11).

A new therapeutic modality that minimizes damage to normal cells and combines cancer selectivity (including cancer stem cells) with a broad anticancer mechanism would represent a paradigm shift in cancer treatment. Naturally occurring phospholipid ethers (PLE) selectively accumulate in human cancer cells compared to normal cells (12–14). Structure-activity relationship studies were previously performed at the University of Michigan with radioiodinated aryl PLE and a subset of alkylphosphocholine (APC) derivatives to see how

alterations in molecular structure affected tumor retention of these compounds (15–18). These studies indicated that, for glycerol-derived PLE analogs, the stereochemistry at the *sn*-2 position of glycerol did not affect tumor uptake and retention in a rat sarcoma model. The length of the hydrophobic alkyl chain was discovered as another key characteristic that affected tumor retention of these compounds. Decreasing the alkyl chain length from 12 carbons (C_{12}) to C_7 resulted in little or no tumor accumulation, whereas increasing the chain length had the opposite effect, with C_{15} and C_{18} analogs showing delayed plasma clearance and enhanced tumor uptake. Furthermore, in the C_{12} APC series, substitution of the choline part of the molecule with ethanol, ethanolamine, or 3,3-dimethyl-1-butanol reduced tumor uptake. From these studies, we found that the glycerol backbone was not required for tumor avidity, the alkyl chain must contain >11 methylene groups, and the position of iodine on the phenyl ring did not influence tumor uptake or specificity.

Ultimately, CLR1404 [18-(*p*-iodophenyl)octadecyl phosphocholine] was identified among nine PLE and APC analogs as the best tumor-imaging agent in rodent models (18). In follow-up pharmacologic toxicology studies, CLR1404 additionally exhibited low rodent toxicity and lower liver, kidney, bladder, and abdominal exposure compared to other derivatives. Moreover, replacement of iodine with optically active moieties yielded similar tumor selectivity and retention, suggesting bulk structural tolerance in that location. Therefore, we hypothesized that the CLR1404 chemical scaffold (Fig. 1) is uniquely well suited to deliver radioiodine isotopes and other reporters that are useful for either diagnostic imaging or therapy for a broad spectrum of solid tumors.

Unlike classical DNA-targeted cytotoxic agents, alkylphospholipids, including APC, target cellular and intracellular membranes (19). When administered at therapeutic doses, alkylphospholipids inhibit phosphatidylcholine biosynthesis, interfere with lipid transduction pathways, and block the endoplasmic reticular transport of cholesterol, thereby ultimately disrupting cholesterol homeostasis and membrane lipid raft function (20). Lipid rafts are specialized plasma membrane microdomains rich in cholesterol and sphingomyelin (21), which spatially organize signaling pathways and regulate cell proliferation and survival (apoptosis) (22). Lipid rafts, which are more abundant in cancer cells relative to normal cells (23), serve as cellular portals of entry for CLR1404 and other alkylphospholipids into tumors.

Here, we report results of in vitro and in vivo testing with radioisotope-labeled CLR1404 for diagnostic imaging (^{124}I-CLR1404) and for cancer therapy (^{131}I-CLR1404), as well as imaging data with the fluorescent analog CLR1501, in a wide variety of tumor models. We also present first-in-human imaging results showing that CLR1404 has tumor-targeting and retention properties in cancer patients. CLR1404 represents a new class of synthetic APC analogs to be used for broad-spectrum, tumor-selective molecular imaging and therapy in human cancers.

RESULTS

Preferential uptake and retention of APC analogs in cancer cell lines

CLR1501, a fluorescently labeled CLR1404 analog (Fig. 1), was administered to seven different cancer cell lines (renal, colorectal, glioma, ovarian, pancreatic, melanoma, and prostate) and a normal human skin fibroblast line in vitro. Twenty-four hours later, CLR1501 exhibited five- to ninefold preferential uptake in these cancer cell lines in vitro compared to normal fibroblasts (Fig. 2A and fig. S1). Retained CLR1501 was associated with plasma and organelle membranes. Cancer-selective localization of APC analogs was also observed in a coculture of human prostate carcinoma cells (PC-3) and a primary normal human skin fibroblast cell line treated with CLR1501 for 24 hours and imaged with confocal microscopy (Fig. 2B).

To further examine cancer cell–selective targeting, three pairs of patient-matched normal and cancer cell lines were treated with ^{125}I-CLR1404. The osteosarcoma cell line 704.T is from the same patient as the normal skin cell line, 704.sk. There was a 2.8-fold increase in the observed ^{125}I-CLR1404 uptake by the osteosarcoma cell line compared to normal, patient-matched cells (Fig. 2C). Similarly, for two non–small cell lung cancer (NSCLC) patient cell lines, H2122 and H1395, there were significant increases in ^{125}I-CLR1404 uptake compared to their patient-matched normal cell lines BL2122 and BL1395 (derived from their respective B-lymphoblast cell lines), respectively.

Next, we visualized the kinetics of CLR1501 entry into PC-3 cells over the course of 1 hour. CLR1501 entered cells via plasma membranes and collected in membrane-bound vesicles, eventually localizing to membranes of cytoplasmic organelles (movie S1). Maximal uptake of ^{125}I-CLR1404 was reached after 48 hours in normal skin fibroblasts compared with 24 hours in human NSCLC cells, with the final levels of ^{125}I-CLR1404 uptake about fourfold higher than observed in normal cells (fig. S2). Pretreatment of PC-3 cells with filipin III, an agent that sequesters cholesterol and disrupts lipid rafts, resulted in nearly 40% less uptake of ^{125}I-CLR1404 compared to untreated control cells (fig. S3). This supports the hypothesis that CLR1404 uses lipid rafts as portals of entry into cancer cells. Notably, higher filipin III concentrations are cytotoxic, and therefore, complete lipid raft ablation (and presumably complete CLR1404 analog uptake inhibition) could not be accomplished.

Because of their emerging role in cancer progression and relapse, cancer stem cells were also analyzed for CLR1404 uptake. Human glioblastoma (GBM) stem-like cell (GSC) lines were isolated from patient surgical specimens. Six GSC lines (12.1, 22, 33, 44, 99, and 105) were validated for enhanced expression of stem cell markers [cluster of differentiation 133 (CD133) and nestin] and multilineage potential (neuronal and glial) (11, 24). Patient-matched, serum-cultured GBM cell lines (serGBM) 22, 33, and 99 were established from the same specimens used for establishing the GSC lines. The stem-like properties of GSCs are rapidly lost in serum culture, so serGBM lines served as a model of non-GSC GBM cells. Both GSCs and serGBM cells exhibited enhanced CLR1501 uptake compared to normal human astrocytes and fetal human neural stem cell (NSC) lines (Fig. 3, A and B). Flow cytometry confirmed greater uptake for GSC and serGBM lines compared to astrocytes (Fig. 3B).

Although enriched for GSCs, GBM spheres consist of a mixture of GSCs, as well as non-GSCs. Therefore, we sought to further verify that GSCs are labeled with CLR1404 analogs by colabeling with the GSC marker CD133. CLR1501 uptake was seen in both $CD133^+$ and $CD133^-$ GSCs; however, significantly higher fluorescence was found in $CD133^+$ GSCs compared to $CD133^+$ NSCs (Fig. 3C and fig. S4). These data indicate that APC analogs preferentially label all GBM cells, including cancer stem-like cells, with minimal retention by normal neural and neural stem cells.

Selective uptake and retention of APC analogs in tumors

Radioiodinated ^{124}I-CLR1404 was tested in subcutaneous and orthotopic xenografts of 57 different spontaneous, transgenic, human, and rodent malignant cell lines and tumor types. After intravenous administration, ^{124}I-CLR1404 localized in almost all primary and metastatic malignant tumors regardless of anatomic location (table S1). Representative examples are of both human (Fig. 4A) and rodent (Fig. 4B) tumors. Pronounced and sustained tumor accumulation was seen by 24 hours in a human prostate cancer xenograft (PC-3), with continued clearance from healthy tissue evident between 48 and 120 hours (fig. S5A). Although liver metastases from all other cancer types were successfully visualized, flank xenografts of two human hepatocellular carcinoma lines did not show prolonged retention (table S1).

In vivo cancer stem cell labeling with CLR1501 was also demonstrated in GSC-derived orthotopic xenografts in mice. After MRI verification of brain tumor, CLR1501 administered intravenously labeled all tumor cells (Fig. 5, A and B), including GSCs that stained positive for nestin, Olig2, and CD15/SSEA-1 (Fig. 5, C to E). These results were verified using ex vivo flow cytometry analysis of CD133 expression in GBM xenograft cells. Subpopulations of $CD133^+$ glioma cells (2 to 26%) were detected in the xenografts of three distinct human-derived GBM lines (U251 glioma, 22 GSC, and 105 GSC). A high fraction of $CD133^+$ GBM cells were colabeled with CLR1501 (Fig. 5, F and G). Notably, a small percentage of $CD133^+$ cells may be retained in the serum-cultured U251 glioma line (25), and serum-cultured tumor lines may reexpress CD133 after in vivo engraftment (26). Therefore, the presence of $CD133^+$ U251 cells within mouse brain tumor xenografts is not unexpected.

Benign or premalignant tumors showed very little or no uptake in animal models (table S1). Moreover, unlike ^{18}F-fluorodeoxyglucose (^{18}F-FDG), a common positron emission tomography (PET) agent for tumor imaging, CLR1404 analogs were not seen in either inflammatory (fig. S5B) or premalignant lesions (table S1). Mean inflammatory lesion–to–tumor ratio was 4.94 with ^{18}F-FDG and 0.34 for CLR1404. Using non-invasive dual-modality PET/CT (computed tomography) colonoscopy and ^{124}I-CLR1404, we visualized both premalignant colonic adenomatous polyps and malignant adenocarcinomas that spontaneously develop in a Pirc rat model (fig. S6). Three-dimensional (3D) micro-PET/CT scanning performed 24 hours after intravenous injection of ^{124}I-CLR1404 revealed PET enhancement of one histologically confirmed malignant adenocarcinoma, but little or no uptake in 19 coexisting premalignant adenomas (movie S2).

Radiotherapy with ^{131}I-CLR1404 in human tumor xenograft models

Owing to observed selective uptake into cancer cells compared to normal cells, coupled with the well-established efficacy of ^{131}I-based molecular radiotherapy in multiple cancer types [such as thyroid cancer, neuroblastoma, non-Hodgkin's lymphoma, and hepatocellular carcinoma (27–29)], ^{131}I-CLR1404 was evaluated in human tumor xenograft models of clear cell renal carcinoma (Caki-2), colorectal carcinoma (HCT-116), ovarian adenocarcinoma (Ovcar-3), triple-negative breast adenocarcinoma (MDA-MB-231), uterine sarcoma (MES-SA/Dx5), glioma (U87-MG), pancreatic carcinoma (Mia Paca-2), and prostate carcinoma (PC-3). A single, nonoptimized intravenous dose of 100 to 145 μCi of ^{131}I-CLR1404 was sufficient to provide statistically significant tumor growth suppression and survival benefit in these cancer models when compared to control animals treated with an equivalent mass dose of nonradioactive CLR1404. Antitumor efficacy was pronounced in terms of the degree and duration of growth suppression in the renal, colorectal, ovarian, prostate, and triple-negative breast cancer models (Fig. 6). In the relatively radioresistant uterine sarcoma and glioma models, two injections of ^{131}I-CLR1404 on days 0 and 20 or 0 and 7, respectively, prevented tumor growth and prolonged survival (fig. S7). These data suggest that tumor delivery of therapeutic ^{131}I with CLR1404 afforded survival benefit in most tumor models after a single treatment.

Tumor imaging with ^{124}I-CLR1404 and ^{131}I-CLR1404 in human cancer patients

After successful imaging and therapy in rodent models of human cancer, we started human trials (table S2) of PET/CT imaging with CLR1404. Preliminary results were obtained in an NSCLC patient without neurological symptoms using ^{124}I-CLR1404 PET/CT. Imaging revealed three previously unknown brain lesions highly suspicious for metastases that were subsequently confirmed with gadolinium-enhanced MRI (Fig. 7A). Clinical management of this patient was then altered to include brain radiotherapy.

Although MRI revealed the suspected grade IV glioma in a patient (Fig. 7, B and C), high tumor–to–normal brain ratios after administration of ^{124}I-CLR1404 also permitted easy tumor visualization (Fig. 7D). In another example, a tumor/brain ratio of 30 on PET was obtained 2 days after injecting 5 mCi of ^{124}I-CLR1404 in a patient with grade II/III astrocytoma (fig. S8). Tumor uptake and prolonged retention were also demonstrated using SPECT (single-photon emission computed tomography)/CT imaging in a colorectal cancer patient with known liver and lung metastases 21 days after injection of ^{131}I-CLR1404 (fig. S9).

We also successfully isolated and expanded GSCs (line 107) from a surgical GBM specimen obtained after preoperative ^{124}I-CLR1404 injection (Fig. 7D). After implantation of 107 GSCs into immunodeficient mice, resultant tumor xenografts were visualized after injection of CLR1502 (near-infrared CLR1404 analog) (Fig. 7E). Highly invasive glioma xenograft phenotypes were also verified after histological processing (Fig. 7, F to I).

DISCUSSION

We demonstrate in vitro and in vivo selective uptake of APC-based imaging and therapeutic agents by a wide range of malignant cells. For in vivo studies, both rodent cancer models and human patients were studied using analogs containing either a PET-imaging isotope (^{124}I) or a SPECT imaging, therapeutic isotope (^{131}I). The cancer cell–selective targeting properties of CLR1404 make it an ideal candidate for both diagnostic and therapeutic applications, thereby illustrating the tandem imaging and therapy paradigm for this versatile APC-based chemical scaffold. As a cancer drug delivery vehicle, its broad-spectrum applicability represents an advance over other more narrowly targeted delivery mechanisms, such as antibodies and peptides. Furthermore, in the case of structurally identical ^{124}I-CLR1404 and ^{131}I-CLR1404, it represents a perfectly matched diagnostic/therapeutic pairing for personalizing and optimizing cancer therapy—with ^{124}I-CLR1404 serving in the diagnostic/imaging capacity for predicting, planning, and following the potential therapeutic efficacy of ^{131}I-CLR1404. Similar to radioiodinated CLR1404 analogs, the fluorescent derivative, CLR1501, also displayed selective uptake and retention in various human cancer cell lines in vitro and in malignant tumors in vivo compared to normal human cells or tissues.

Uptake of the CLR1404 chemical scaffold into cancer cells appears to partially involve interaction with lipid raft regions of the plasma membrane (22, 30–32). This hypothesis was supported in this study by decreased uptake of ^{125}I-CLR1404 after pretreatment of human cancer cells with the lipid raft disruptor, filipin III. A lipid raft–based mechanism for uptake into cancer cells has also been reported for other alkylphospholipids (21). Lipid rafts and cholesterol (a key raft constituent) are more abundant in cancer cells compared to normal cells (23), and may partially account for CLR1404's cancer cell selectivity. CLR1404 interaction with lipid rafts may also explain the finding that CLR1404 uptake was significantly higher in CD133^{+} GSCs versus matched CD133^{-} non-GSCs (in four of five sphere-cultured lines), because CD133 was demonstrated to localize to cholesterol-rich lipid raft microdomains (33).

PET/CT imaging of a wide range of in vivo rodent cancer models using CLR1404 derivatives showed cancer-selective uptake and retention. Notably, these models include genetically engineered tumors and spontaneous tumors, in addition to human tumor xenograft models (subcutaneous and orthotopic). Exploiting the sensitivity and quantification properties of PET, ^{124}I-CLR1404 imaging revealed both primary cancers and metastatic lesions in these models. Malignant tumor selectivity was confirmed in tissue distribution studies with ^{125}I-CLR1404 in multiple animal tumor models (18).

Initial imaging results obtained with ^{124}I-CLR1404 in a small number of human lung and brain cancer patients confirmed tumor uptake and retention properties seen in preclinical models. Tumor conspicuity was particularly marked because of the combination of high brain tumor uptake (primary gliomas and brain metastases) and low normal brain background radioactivity. ^{124}I-CLR1404 holds promise as a broadly applicable diagnostic PET imaging tool with widespread oncology indications. In addition to its potential use for detecting and staging cancer (including total tumor burden and metastases), the 4-day

radioactive half-life of ^{124}I-CLR1404 may enable early postoperative PET imaging to detect and quantitate any remaining tumor cells after resections. Furthermore, ^{124}I-CLR1404 may offer several important advantages over the current state-of-the-art oncology PET imaging agent, ^{18}F-FDG. These include greater specificity for cancer cells (^{18}F-FDG accumulates in all tissues that metabolize glucose at a relatively high rate, including tumors, inflammation, and normal brain), application to a broader range of cancer types, and logistical advantages due to a substantially longer radioactive half-life (^{124}I-CLR1404 = 4 days versus ^{18}F-FDG = 110 min).

The versatility of the APC-based chemical scaffold was further illustrated by the therapeutic ^{131}I-CLR1404 radioisostere. ^{131}I is a well-established cytotoxic radioisotope. Treatment efficacy, measured as tumor growth suppression and survival extension, was demonstrated in a wide range of human tumor xenograft models, some after only a single intravenous dose. Patient data showed preferential uptake and prolonged tumor retention of ^{131}I-CLR1404 compared to surrounding normal tissues (including bone marrow). Thus, ^{131}I-CLR1404 combines a powerful and widely applicable therapeutic modality (radiation) with a broad-spectrum cancer-targeting mechanism.

To better understand and translate these APC analogs to clinical use, other questions need to be addressed. Cancer and cancer stem cell–specific uptake and retention of CLR1404 analogs in other cancer types need to be verified, beyond the GSC and GBM data in this study. For central nervous system (CNS) tumor therapy, the blood-brain barrier (BBB) permeability of CLR1404 analogs remains unknown. Primary or metastatic brain tumors often alter BBB permeability and other vascular properties (34), which may enhance the permeability of CLR1404 analogs. Minimal uptake and retention in normal brain both in animal models and in humans suggest a low CLR1404 analog permeability across intact BBB; alternatively, normal neural tissues may also metabolize CLR1404 analogs more rapidly than other body tissues. Optimal dosing and imaging parameters for human imaging and therapy for different cancers (that is, primary versus metastatic, body versus brain tumors), and relative to patient weight, age, or other physical parameters, need to be investigated.

In conclusion, the APC analog–based scaffold exemplified by CLR1404 can act as a cancer cell and cancer stem cell–targeted vehicle for diagnosis and therapy in many types of malignant tumors. They may discriminate tumor recurrence versus pseudoprogression, a difficult task with current imaging technologies. Optical CLR1404 analogs may find additional use in intraoperative applications.

MATERIALS AND METHODS

Study design

Our goal was to evaluate the use of CLR1404 APC analogs in tumor imaging and therapy. We tested radioiodinated and fluorescent CLR1404 analogs (Fig. 1) for tumor-specific labeling and retention properties in vitro and in vivo in 57 different tumor cell lines and xenograft and transgenic tumor models, and also tested whether tumor labeling is altered by lipid raft disruption. Using six distinct human GSC lines, we tested the ability of APC

analogs to label both cancer stem cells and serum-cultured, non–stem cells from GBM. Then, we showed the efficacy of ^{131}I-CLR1404 therapy in animal tumor models of eight different human cancers. We also evaluated the use of APC analogs in human cancer imaging in adult patients with different types of primary and metastatic cancers throughout the body and brain (table S2) through the following clinical trials registered on clinicaltrials.gov: NCT01516905, NCT01540513, NCT01495663, NCT00582283, and NCT01898273.

Synthesis and radioiodination of CLR1404

Synthesis of 18-(*p*-iodophenyl)octadecyl phosphocholine was previously reported (18). Radioiodination was achieved in 70% isolated radiochemical yield via isotope exchange with ^{124}I–(IBA Molecular North America), ^{125}I–, or ^{131}I–sodium iodide (PerkinElmer) (35). After purification (>99% radiochemical purity) and accurate mass quantification by high-performance liquid chromatography [normal phase, isocratic isopropanol/hexanes/water (13:10:2)], the radiopharmaceutical was dissolved in absolute ethanol (50 to 500 μl) and Tween 20 (0.1 μl/μg of compound).The ethanol was removed under vacuum, and the residue was dissolved in sterile water to give a final solution containing no more than 0.4% Tween 20. Sterilization is achieved by filtration through a sterile 0.2-μm filter unit. Injection solutions are tested for pyrogens using the Limulus Amebocyte Lysate test kit. Synthesis of the other analogs, CLR1501 and CLR1502, is shown in fig. S10 and described in Supplementary Methods.

Cell culture

Human cancer cell lines were purchased from the American Type Culture Collection (ATCC). They included the following: Caki-2 (renal; clear cell carcinoma), HCT-116 (colorectal carcinoma); MES-SA/Dx5 (uterine sarcoma) [all maintained in McCoy's 5a medium supplemented with 10% fetal bovine serum (FBS)], Ovcar-3 (ovarian adenocarcinoma) [maintained in RPMI medium supplemented with 20% FBS], U87-MG (glioma) [maintained in minimum essential medium supplemented with 10% FBS], Mia Paca-2 (pancreatic carcinoma) (maintained in Dulbecco's modified Eagle's medium supplemented with 10% FBS), PC-3 (prostate carcinoma) (maintained in F-12K medium supplemented with 10% FBS), MDA-MB-231 (triple-negative mammary gland adenocarcinoma) (maintained in Leibovitz's medium supplemented with 10% FBS), and A549 (non–small cell lung carcinoma) (maintained in F-12 medium supplemented with 10% FBS). Normal human skin fibroblasts were purchased from ATCC and grown in Fibroblast Basal Medium PCS-201-030 supplemented with serum-free kit (Fibroblast Growth Kit-Serum-Free PCS-201-040). All media (except for MDA-MB-231 cell line) also contained penicillin (100 U/ml) and streptomycin (100 μg/ml) and were maintained at 37°C with 5% CO_2 in air.

Fluorescent staining and confocal imaging

All cells were maintained at 37°C in appropriate medium supplemented with 10% FBS and 5% CO_2. Before imaging, the cells were removed from flasks with 0.25% trypsin and were allowed to grow overnight on the microslides VI (Ibidi). The next day, the cells were

washed with phosphate-buffered saline (PBS) and were incubated with either 5 or 7.5 μM (as indicated) of CLR1501 in appropriate serum-free medium for 24 hours. CLR1501 was formulated with 0.4% of Polysorbate 20, 2% of ethanol, and saline. After washing thoroughly with PBS, the cells were imaged using Bio-Rad Radiance 2100 MP Rainbow laser scanning/multiphoton confocal microscope using a 1-s exposure time. Alternatively, cells were visualized using a Nikon A1R confocal microscope (Keck Laboratory, University of Wisconsin-Madison). The emission signal of CLR1501 was detected using Alexa Fluor 488 filters (ex/em 480/520 nm).

Cell culture videography

PC-3 cells, a human prostate adenocarcinoma, were maintained in F12 medium supplemented with 10% FBS and 1% penicillin and streptomycin. The cells were plated overnight in MatTek petri dish. The next day, the cells were washed with PBS and stained with Image-IT LIVE Mitochondrial and Nuclear Labeling Kit, which provides two stains—red fluorescent MitoTracker Red CMXRos dye and blue-fluorescent Hoechst 33342 dye—for highly selective mitochondrial and nuclear staining (Invitrogen). The image acquisition was performed with an A1R Nikon confocal system and was initiated when 5 μM CLR1501 was added to the petri dish; the video (movie S1) was acquired for 1 hour.

Matched cell lines

Three sets of normal human and cancer cell lines were purchased from ATCC. The lung adenocarcinoma cell line (NCI-H1395) and a normal B-lymphoblast cell line derived from the same patient (NCI-BL1395) were both cultured in RPMI 1640 medium supplemented with 10% FBS. The NSCLC cell line (NCI-H2122) and a normal B-lymphoblast cell line derived from the same patient (NCI-BL2122) were also both cultured in RPMI 1640 medium supplemented with 10% FBS. The osteosarcoma cell line (Hs 704.T) and a normal skin fibroblast cell line derived from the same patient (Hs 704.sk) were both cultured in Dulbecco's modified Eagle's medium supplemented with 10% FBS. Uptake and retention of ^{125}I-CLR1404 at 24 hours were determined as described above.

Isolation of GSCs

GSCs were isolated and propagated using marker neutral, serum-free sphere culture in stem cell medium following protocols previously reported (11, 24), under an approved institutional review board protocol. Using this methodology, we isolated and fully validated six GSC lines, five primary and one recurrent: 12.1 (recurrent), 22, 33, 44, 99, and 105. These different GSC lines exhibit varied molecular and biological properties (24). Human cortex fetal NSCs were maintained as previously described (36). SerGBM and normal human astrocytes were maintained in medium containing 10% FBS.

Human tumor xenograft models

All described animal studies were performed according to animal protocols approved by the Institutional Animal Care and Use Committee. Female athymic nude mice (Hsd:Athymic Nude-Foxn1nu or Crl:NU-Foxn1nu, Charles River Laboratories) about 4 to 5 weeks of age, 16 to 18 g (n = 6), were used for human tumor xenograft studies. Mice were anesthetized

with isoflurane and injected subcutaneously with viable tumor cells in 100 μl of Dulbecco's PBS (or, for glioma cells, 50 μl of PBS) into the right flank. Inoculum sizes were 1×10^6 (for renal, ovarian, glioma, pancreatic, prostate, and NSCLC models), 2×10^6 (for colorectal and uterine models), or 3×10^6 (breast).

Radiotherapy of tumor-bearing mice

Both ^{131}I-CLR1404 and the control, CLR1404, were formulated with 0.08% Polysorbate 20 NF, 0.4% sodium ascorbate USP, 5% ethanol, 200 proof, USP in 0.9% sodium chloride injection, USP. The formulation for the glioma and breast models used 25% ethanol. At the time of dose preparation, the drug formulation was diluted 1:5 in 0.9% sodium chloride to reduce the ethanol concentration to about 5%. For assessment of CLR1404, formulation was in 0.08% of Tween 20, 0.4% sodium ascorbate USP, 5% ethanol in 0.9% NaCl for injection, USP. The control was 0.9% NaCl for injection, USP. Treatment with test agents via tail vein injection (150 μl of dosing volume) was initiated when tumors had reached a predetermined size range in mm^3 (50 to 150 for uterine, pancreatic, glioma, and breast; 50 to 230 for ovarian; 100 to 150 for NSCLC; 100 to 250 for renal and colorectal; and 150 to 300 for prostate). Once tumors reached these target ranges, animals were randomly assigned to treatment groups (day 0).

In ^{131}I-CLR1404–treated animals, the approximate radioactivity dosed per mouse (administered on day 0 only, unless otherwise indicated) and the number of mice per group were as follows: renal: 110 μCi, $n = 6$; colorectal: 110 μCi, $n = 6$; uterine: day 0, 130 μCi, and day 20, 145 μCi, $n = 6$; ovarian: 115 μCi, $n = 5$; glioma: days 0 and 7, 100 μCi, $n = 8$; pancreatic: 125 μCi, $n = 5$; prostate: day 7, 100 μCi, $n = 6$; breast: day 7, 100 μCi, $n = 8$ to 9. Control animals ($n = 6$) were administered 0.0038 mg of CLR1404 (~0.19 mg/kg, an amount equivalent to that represented by a 100-μCi dose of ^{131}I-CLR1404) on day 0 only. In all therapy studies, mice were given potassium iodide at a concentration of 0.1% in their drinking water to block uptake of any free iodide in the drug formulation [with the addition of 0.4% (w/v) sweetener (Sweet and Low) to aid palatability] starting 3 days before the estimated day 0 for a total of 17 days. All mice were given free access to food and water throughout each study. The nonradioactive animals were housed in groups of three to four in cages and well separated from the radioactive animal cages. Radioactive animals were housed individually with lead shielding between cages.

Tumor growth was assessed by measuring two perpendicular tumor diameters using a caliper, and the resulting measurements were used for estimating tumor volume [tumor volume = $(\text{width}^2 \times \text{length} \times \pi)/6$]. Survival analysis was based on the date of death of the animal, or the date the animal was sacrificed based on either being found in moribund condition or the tumor size reaching >2000 mm^3.

In vivo micro-PET/CT imaging

Mice were anesthetized with isoflurane (2%) and scanned in a prone position on a Siemens Inveon micro-PET/CT scanner (Siemens Preclinical Systems) at various time points (ranging from 6 hours to 10 days) after injection of ^{124}I-CLR1404 (80 to 150 μCi). CT scans were acquired with an x-ray energy of 70 kVp at 1000 mA for 200 ms with 220° of rotation

and 220 back-projections. CT images were reconstructed with filtered back-projection using system software with a Shepp-Logan filter to voxel sizes of $0.2 \times 0.2 \times 0.2$ mm^3. PET scans were acquired for 10 to 30 min (40 to 100 million counts) and reconstructed with either 2D-OSEM (2D ordered–subset expectation–maximization) with 16 subsets and 4 EM (expectation maximization) iterations or 3D-OSEM with 16 subsets and 18 iterations to voxel size of $0.8 \times 0.8 \times 0.8$ mm^3. Corrections of normalization, dead time, scatter, and attenuation were applied using the system software and the co-registered CT scan. PET data were quantified using a calibration specific to ^{124}I. Image analysis, including region of interest quantification and co-registration of multiple time points, was performed with the Inveon Research Workplace (Siemens Preclinical Systems) and Amira (Visage Imaging Inc.).

Micro-PET tumor imaging with ^{124}I-CLR1404 and ^{18}F-FDG in the presence of inflammation is described in Supplementary Methods.

GSC orthotopic xenograft model

All described animal studies were performed according to animal protocols approved by the Institutional Animal Care and Use Committee. GSC-derived orthotopic xenografts were initiated as previously described (11, 24). Cells were stereotactically injected into the right striatum of anesthetized nonobese diabetic severe combined immunodeficient mice at the following coordinates referenced from bregma: 0 mm anteroposterior, +2.5 mm mediolateral, and −3.5 mm dorsoventral. Mice were then euthanized upon tumor verification by MRI or onset of neurological symptoms, and brain was processed for histological analysis.

In vivo optical studies

Fluorescent analog CLR1501 (green) or CLR1502 (near-infrared) was injected (1 mg) intravenously (lateral tail vein) or retro-orbitally into anesthetized (isoflurane) mice bearing orthotopic GSC-derived xenografts. After 4 days, animals were euthanized and brains were excised, fixed, frozen-sectioned, and immunohistochemically stained as described above. Confocal microscopy was then performed as described above. CLR1502 was visualized using IVIS Spectrum system (PerkinElmer/Xenogen).

Human PET/CT imaging

Human PET brain scans were acquired on a 64-slice PET/CT scanner (Discovery VCT, General Electric) at multiple time points after the injection of about 5 mCi of ^{124}I-CLR1404 using a 90-min dynamic acquisition sequence (2D, nine frames at 10 min each, VIP list mode on) and reconstructed [Advantage Workstation version AW4.4, General Electric, 30 cm DFOV (display field of view), 128 × 128, OSEM VUE Point, 10 subsets with two iterations, standard *z* axis, attenuation correction and dead time, scatter, and decay correction].

SPECT/CT images of ^{131}I-CLR1404 in human cancer patients

After the injection of ^{131}I-CLR1404, planar whole-body images at multiple time points were acquired on a dual-head scanner (Infinia Hawkeye, General Electric) using a scan speed of

10 cm/s, 256 × 1024 matrix, peak set at 364 keV ± 15% and scatter peaks of 312 keV ± 15% and 424 keV ± 15%, high energy all-purpose collimator, and display bone dual density. SPECT/CT images of specific regions of interest were acquired at multiple time points on a SPECT/CT scanner (Infinia Hawkeye, General Electric) using 128 × 128 matrix, 120 projections, 3° per stop, 30 s per stop, with peak set at 364 ± 15% and scatter peaks of 312 ± 15% and 424 ± 15%. The CT settings are helical using a pitch of 1.9, interval 4.42 mm, voltage 140 kV, current 2.5 mA, matrix 512 × 512, filter soft, and pixel 1.10 mm. Processing was performed with Volumetrix MI.

Statistics

One-way repeated measurement ANOVA (SigmaStat v3.5, Systat Software Inc.) was performed to analyze tumor growth in control and treatment groups. Tumor growth was plotted until one animal from either group died (to maintain appropriate statistical analysis). A log-rank statistical analysis was used for comparison of survival benefit between groups. All comparisons of multiple groups were performed with one-way ANOVA with Bonferroni post hoc testing. $P < 0.05$ was considered significant.

Supplementary Material

Refer to Web version on PubMed Central for supplementary material.

Acknowledgments

L. Rodenkirch was helpful in obtaining the confocal microscopy images, and A. Nomura assisted with animal model maintenance. We appreciate advice and the Pirc rat model from W. Dove.

Funding: Clinical brain tumor imaging was supported by the National Cancer Institute (NCI) (RO1-158800) and an UW Institute for Clinical and Translational Research pilot grant (9U54TR000021). Clinical lung cancer imaging and ^{131}I therapy trials were funded by Cellectar Biosciences Inc. J.M.F. was partially supported by NIH training grants [Radiological Sciences T32CA009206, UW MSTP (Medical Scientist Training Program) T32GM008692]. General funding provided by UW Carbone Cancer Center, Wisconsin Partnership Program core grant support of the Center for Stem Cell and Regenerative Medicine, from the University of Wisconsin (Graduate School and Department of Neurological Surgery), and support for J.S.K. from the HEAD-RUSH Brain Tumor Research Professorship and Roger Loff Memorial Fund for GBM Research. Pilot grants and small-animal imaging were supported by the UW Carbone Cancer Center NCI Support grant (P30 CA014520) and the University of Wisconsin (Graduate School, Departments of Radiology, Medical Physics, Human Oncology, and Neurological Surgery, Wisconsin Alumni Research Foundation, and Wisconsin Institutes of Discovery).

REFERENCES AND NOTES

1. Ting G, Chang CH, Wang HE, Lee TW. Nanotargeted radionuclides for cancer nuclear imaging and internal radiotherapy. J. Biomed. Biotechnol. 2010; 2010:953537. [PubMed: 20811605]
2. Tedcastle A, Cawood R, Di Y, Fisher KD, Seymour LW. Virotherapy—Cancer targeted pharmacology. Drug Discov. Today. 2012; 17:215–220. [PubMed: 22198165]
3. Steiner M, Neri D. Antibody-radionuclide conjugates for cancer therapy: Historical considerations and new trends. Clin. Cancer Res. 2011; 17:6406–6416. [PubMed: 22003068]
4. Guo ZS, Thorne SH, Bartlett DL. Oncolytic virotherapy: Molecular targets in tumor-selective replication and carrier cell-mediated delivery of oncolytic viruses. Biochim. Biophys. Acta. 2008; 1785:217–231. [PubMed: 18328829]
5. Kaur S, Venktaraman G, Jain M, Senapati S, Garg PK, Batra SK. Recent trends in antibody-based oncologic imaging. Cancer Lett. 2012; 315:97–111. [PubMed: 22104729]

6. Fernandez-Fernandez A, Manchanda R, McGoron AJ. Theranostic applications of nanomaterials in cancer: Drug delivery, image-guided therapy, and multifunctional platforms. Appl. Biochem. Biotechnol. 2011; 165:1628–1651. [PubMed: 21947761]
7. Lin MM, Kim HH, Kim H, Dobson J, Kim do K. Surface activation and targeting strategies of superparamagnetic iron oxide nanoparticles in cancer-oriented diagnosis and therapy. Nanomedicine. 2010; 5:109–133. [PubMed: 20025469]
8. Bhattacharyya S, Kudgus RA, Bhattacharya R, Mukherjee P. Inorganic nanoparticles in cancer therapy. Pharm. Res. 2011; 28:237–259. [PubMed: 21104301]
9. Bao S, Wu Q, McLendon RE, Hao Y, Shi Q, Hjelmeland AB, Dewhirst MW, Bigner DD, Rich JN. Glioma stem cells promote radioresistance by preferential activation of the DNA damage response. Nature. 2006; 444:756–760. [PubMed: 17051156]
10. Singh A, Settleman J. EMT, cancer stem cells and drug resistance: An emerging axis of evil in the war on cancer. Oncogene. 2010; 29:4741–4751. [PubMed: 20531305]
11. Clark PA, Iida M, Treisman DM, Kalluri H, Ezhilan S, Zorniak M, Wheeler DL, Kuo JS. Activation of multiple ERBB family receptors mediates glioblastoma cancer stem-like cell resistance to EGFR-targeted inhibition. Neoplasia. 2012; 14:420–428. [PubMed: 22745588]
12. Snyder F, Blank ML, Morris HP. Occurrence and nature of O-alkyl and O-alk-I-enyl moieties of glycerol in lipids of Morris transplanted hepatomas and normal rat liver. Biochim. Biophys. Acta. 1969; 176:502–510. [PubMed: 4308118]
13. Snyder F, Wood R. Alkyl and alk-1-enyl ethers of glycerol in lipids from normal and neoplastic human tissues. Cancer Res. 1969; 29:251–257. [PubMed: 5763979]
14. Soodsma JF, Piantadosi C, Snyder F. The biocleavage of alkyl glyceryl ethers in Morris hepatomas and other transplantable neoplasms. Cancer Res. 1970; 30:309–311. [PubMed: 4314993]
15. Rampy MA, Pinchuk AN, Weichert JP, Skinner RW, Fisher SJ, Wahl RL, Gross MD, Counsell RE. Synthesis and biological evaluation of radioiodinated phospholipid ether stereoisomers. J. Med. Chem. 1995; 38:3156–3162. [PubMed: 7636878]
16. Meyer KL, Schwendner SW, Counsell RE. Potential tumor or organ-imaging agents. 30. Radioiodinated phospholipid ethers. J. Med. Chem. 1989; 32:2142–2147. [PubMed: 2769685]
17. Rampy MA, Brown RS, Pinchuk AN, Weichert JP, Skinner RW, Fisher SJ, Wahl RL, Gross MD, Ethier SP, Counsell RE. Biological disposition and imaging of a radioiodinated alkylphosphocholine in two rodent models of breast cancer. J. Nucl. Med. 1996; 37:1540–1545. [PubMed: 8790215]
18. Pinchuk AN, Rampy MA, Longino MA, Skinner RW, Gross MD, Weichert JP, Counsell RE. Synthesis and structure–activity relationship effects on the tumor avidity of radioiodinated phospholipid ether analogues. J. Med. Chem. 2006; 49:2155–2165. [PubMed: 16570911]
19. Kuerschner L, Richter D, Hannibal-Bach HK, Gaebler A, Shevchenko A, Ejsing CS, Thiele C. Exogenous ether lipids predominantly target mitochondria. PLOS One. 2012; 7:e31342. [PubMed: 22348073]
20. van Blitterswijk WJ, Verheij M. Anticancer mechanisms and clinical application of alkylphospholipids. Biochim. Biophys. Acta. 2013; 1831:663–674. [PubMed: 23137567]
21. van der Luit AH, Vink SR, Klarenbeek JB, Perrissoud D, Solary E, Verheij M, van Blitterswijk WJ. A new class of anticancer alkylphospholipids uses lipid rafts as membrane gateways to induce apoptosis in lymphoma cells. Mol. Cancer Ther. 2007; 6:2337–2345. [PubMed: 17699729]
22. Lingwood D, Simons K. Lipid rafts as a membrane-organizing principle. Science. 2010; 327:46–50. [PubMed: 20044567]
23. Li YC, Park MJ, Ye SK, Kim CW, Kim YN. Elevated levels of cholesterol-rich lipid rafts in cancer cells are correlated with apoptosis sensitivity induced by cholesterol-depleting agents. Am. J. Pathol. 2006; 168:1107–1118. [PubMed: 16565487]
24. Zorniak M, Clark PA, Leeper HE, Tipping MD, Francis DM, Kozak KR, Salamat MS, Kuo JS. Differential expression of 2′,3′-cyclic-nucleotide 3′-phosphodiesterase and neural lineage markers correlate with glioblastoma xenograft infiltration and patient survival. Clin. Cancer Res. 2012; 18:3628–3636. [PubMed: 22589395]

25. Qiang L, Yang Y, Ma YJ, Chen FH, Zhang LB, Liu W, Qi Q, Lu N, Tao L, Wang XT, You QD, Guo QL. Isolation and characterization of cancer stem like cells in human glioblastoma cell lines. Cancer Lett. 2009; 279:13–21. [PubMed: 19232461]
26. Peickert S, Waurig J, Dittfeld C, Dietrich A, Garbe Y, Kabus L, Baumann M, Grade M, Ried T, Kunz-Schughart LA. Rapid re-expression of CD133 protein in colorectal cancer cell lines in vitro and in vivo. Lab. Invest. 2012; 92:1607–1622. [PubMed: 22964855]
27. Hackshaw A, Harmer C, Mallick U, Haq M, Franklyn JA. ^{131}I activity for remnant ablation in patients with differentiated thyroid cancer: A systematic review. J. Clin. Endocrinol. Metab. 2007; 92:28–38. [PubMed: 17032718]
28. Pohlman B, Sweetenham J, Macklis RM. Review of clinical radioimmunotherapy. Expert Rev. Anticancer Ther. 2006; 6:445–461. [PubMed: 16503861]
29. Macklis RM, Pohlman B. Radioimmunotherapy for non-Hodgkin's lymphoma: A review for radiation oncologists. Int. J. Radiat. Oncol. Biol. Phys. 2006; 66:833–841. [PubMed: 16965871]
30. Simons K, Sampaio JL. Membrane organization and lipid rafts. Cold Spring Harb. Perspect. Biol. 2011; 3:a004697. [PubMed: 21628426]
31. Kusumi A, Fujiwara TK, Morone N, Yoshida KJ, Chadda R, Xie M, Kasai RS, Suzuki KG. Membrane mechanisms for signal transduction: The coupling of the meso-scale raft domains to membrane-skeleton-induced compartments and dynamic protein complexes. Semin. Cell Dev. Biol. 2012; 23:126–144. [PubMed: 22309841]
32. Staubach S, Hanisch FG. Lipid rafts: Signaling and sorting platforms of cells and their roles in cancer. Expert Rev. Proteomics. 2011; 8:263–277. [PubMed: 21501018]
33. Giebel B, Corbeil D, Beckmann J, Höhn J, Freund D, Giesen K, Fischer J, Kögler G, Wernet P. Segregation of lipid raft markers including CD133 in polarized human hematopoietic stem and progenitor cells. Blood. 2004; 104:2332–2338. [PubMed: 15231568]
34. Wolburg H, Noell S, Fallier-Becker P, Mack AF, Wolburg-Buchholz K. The disturbed blood–brain barrier in human glioblastoma. Mol. Aspects Med. 2012; 33:579–589. [PubMed: 22387049]
35. Mangner TJ, Wu JL, Wieland DM. Solid-phase exchange radioiodination of aryl iodides. Facilitation by ammonium sulfate. J. Organ. Chem. 1982; 47:1484–1488.
36. Svendsen CN, ter Borg MG, Armstrong RJ, Rosser AE, Chandran S, Ostenfeld T, Caldwell MA. A new method for the rapid and long term growth of human neural precursor cells. J. Neurosci. Methods. 1998; 85:141–152. [PubMed: 9874150]
37. Liebeskind LS, Srogl J. Heteroaromatic thioether–boronic acid cross-coupling under neutral reaction conditions. Org. Lett. 2002; 4:979–981. [PubMed: 11893201]
38. Peña-Cabrera E, Aguilar-Aguilar A, Gonzalez-Domínguez M, Lager E, Zamudio-Vazquez R, Godoy-Vargas J, Villanueva-García F. Simple, general, and efficient synthesis of meso-substituted borondipyrromethenes from a single platform. Org. Lett. 2007; 9:3985–3988. [PubMed: 17764191]
39. Goud TV, Tutar A, Biellmann JF. Synthesis of 8-heteroatom-substituted 4,4-difluoro-4-bora-3a,4a-diaza-s-indacene dyes (BODIPY). Tetrahedron. 2006; 62:5084–5091.
40. Kemper K, Sprick MR, de Bree M, Scopelliti A, Vermeulen L, Hoek M, Zeilstra J, Pals ST, Mehmet H, Stassi G, Medema JP. The AC133 epitope, but not the CD133 protein, is lost upon cancer stem cell differentiation. Cancer Res. 2010; 70:719–729. [PubMed: 20068153]

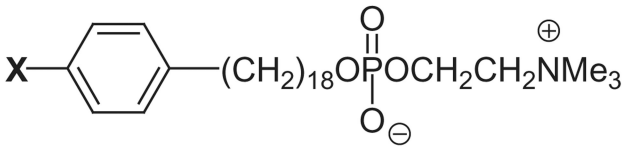

^{131}I-CLR1404	X = ^{131}I	Radioisostere; molecular radiotherapeutic
^{124}I-CLR1404	X = ^{124}I	Radioisostere; PET imaging
^{125}I-CLR1404	X = ^{125}I	Radioisostere
CLR1401	X = ^{127}I	Nonradioactive isostere; chemotherapeutic

CLR1501 X = 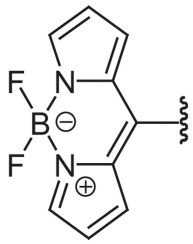 Fluorescent analog

CLR1502 X = 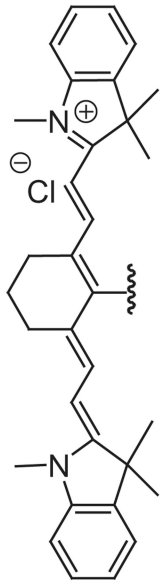 Near-infrared analog

Fig. 1. APC analog chemical structures

CLR1404 could be synthesized as a radioactive compound (^{125}I, ^{124}I, or ^{131}I), as a fluorescent analog (CLR1501), or as a near-infrared analog (CLR1502).

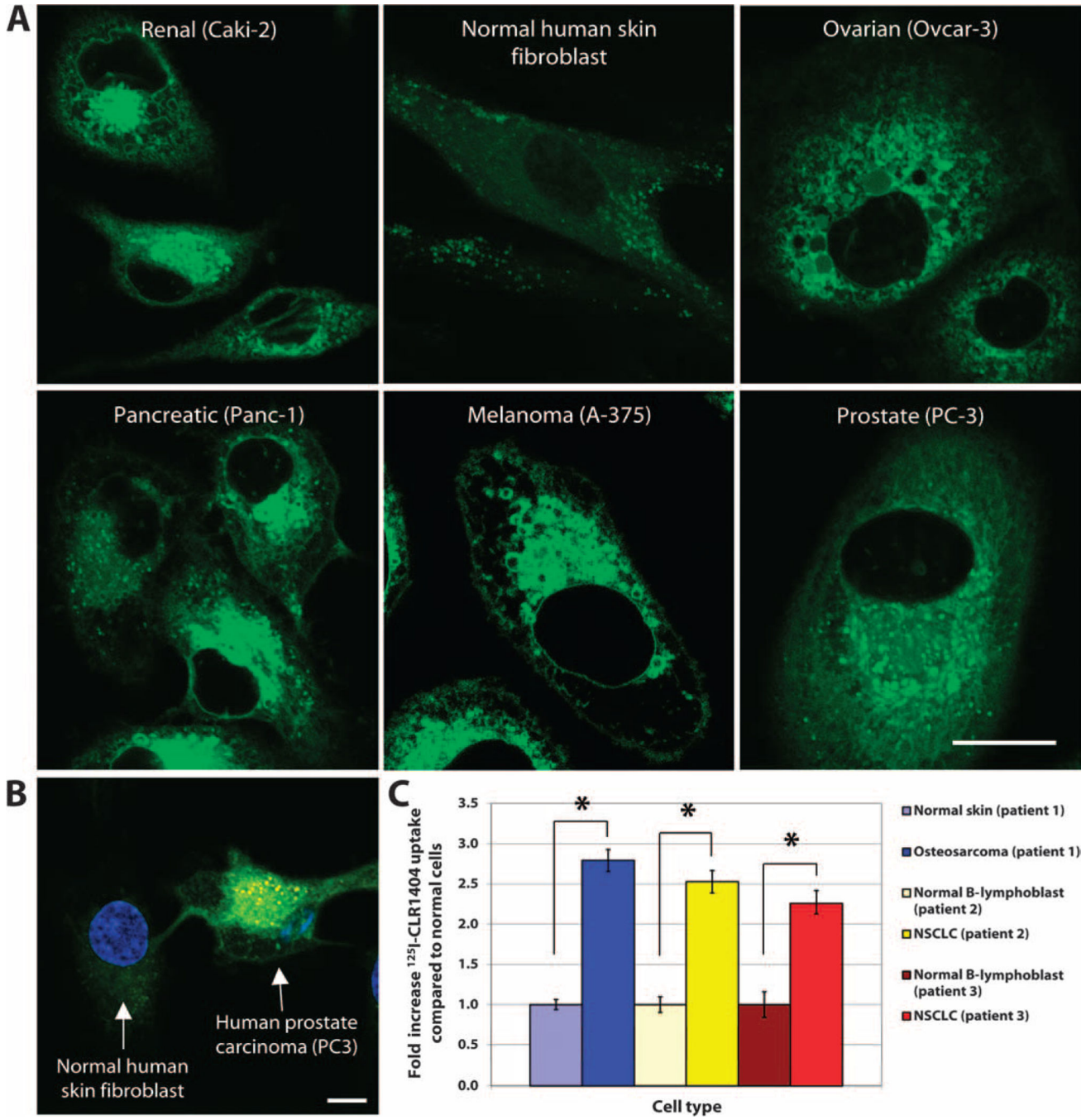

Fig. 2. Uptake of CLR1404 analogs in human cancer cell lines

(**A**) Fluorescence confocal microscopy shows CLR1501 (5 μM) uptake in multiple cancer types, and less uptake in normal human fibroblasts at 24 hours. Scale bar, 10 μm. (**B**) Coculture of human prostate cancer (PC-3) cells and normal human fibroblasts. Cells were treated with the fluorescent analog CLR1501 (5 μM) for 24 hours and counterstained with the nuclear stain, Hoechst 33342. Scale bar, 10 μm. (**C**) Quantitative uptake and retention of ^{125}I-CLR1404 in three cancer cell lines derived from patients and the corresponding patient-matched normal cell lines. Data are means ± SEM (n = 3 independent experiments

with three biological replicates each). *$P < 0.001$, analysis of variance (ANOVA) with post hoc Tukey test.

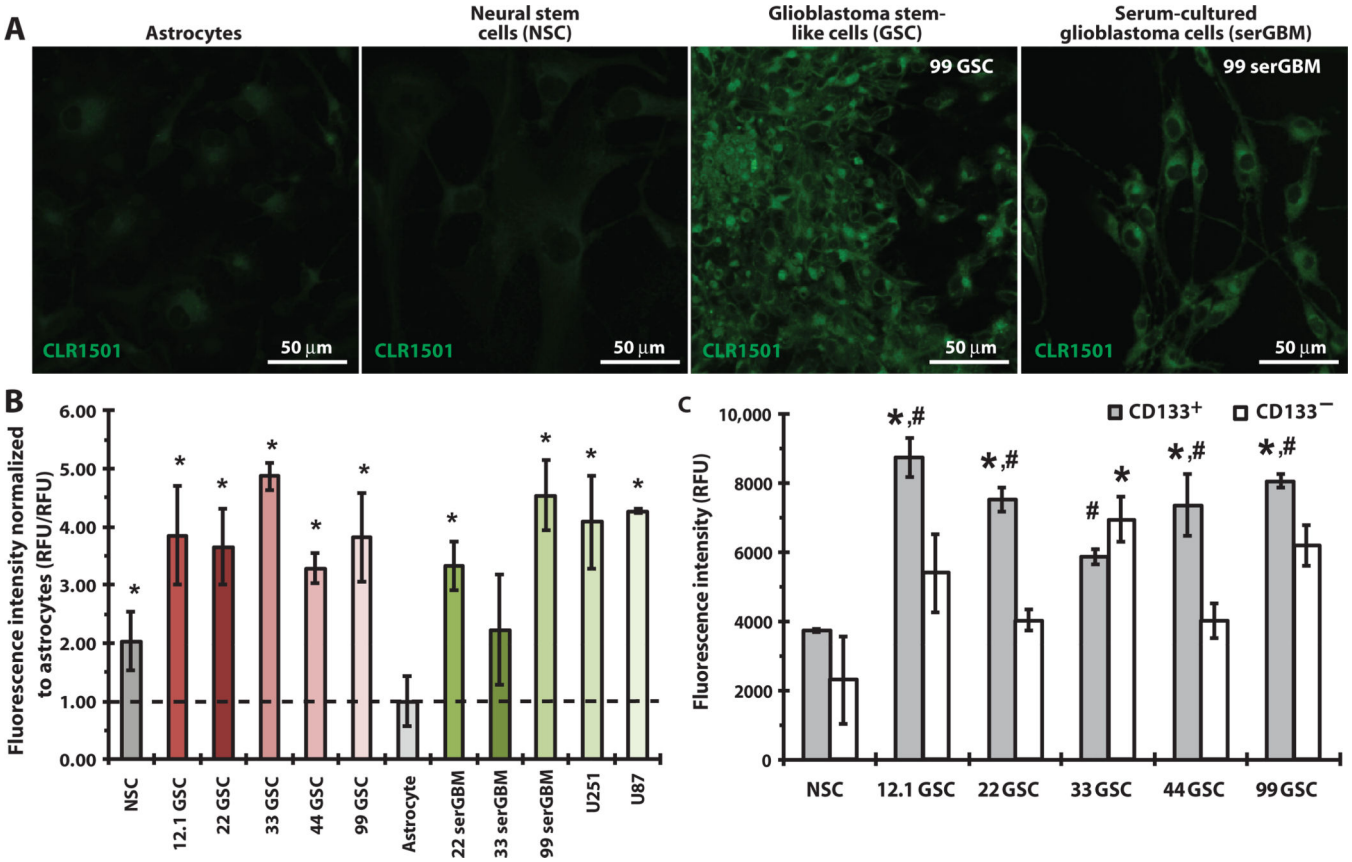

Fig. 3. CLR1501 fluorescent labeling of GSCs in vitro

(**A**) GSCs (line 99) were treated overnight with CLR1501. CLR1501 uptake was visualized with confocal microscopy and compared to matched serGBM, normal human astrocytes, and human NSCs. (**B**) Flow cytometry was performed to quantify CLR1501 uptake after 24 hours in GSC patient–specific lines 12.1, 22, 33, 44, and 99; serGBM lines 22, 33, 99, U251, and U87; NSCs; and astrocytes. Data are means ± SD of three independent experiments. **P* < 0.05, Student's *t* test compared to astrocyte. RFU, relative fluorescence unit. (**C**) CLR1501 labeling of the $CD133^+$ subpopulation of GSCs was analyzed using flow cytometry. Data are means ± SD of three independent experiments. **P* < 0.05 versus line-matched $CD133^+$ or $CD133^-$ cells; $^{\#}P < 0.05$ versus NSCs, Student's *t* test.

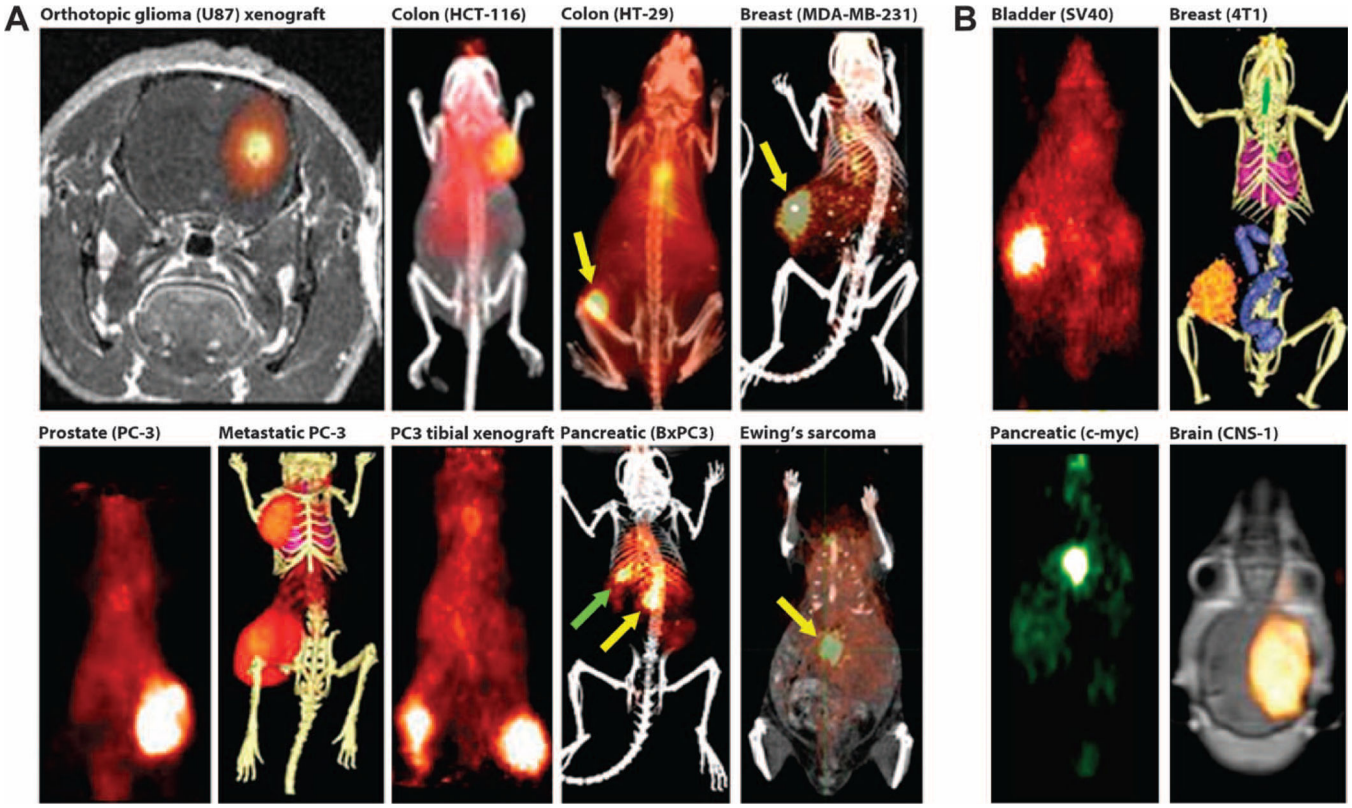

Fig. 4. ^{124}I-CLR1404 uptake in a broad range of tumors

Images shown are micro-PET or PET/CT, or fused brain MRI (magnetic resonance imaging)/PET. Yellow arrows show xenografts; green arrow points to liver metastasis. (**A**) Xenografts of human cancer cell lines: brain (U87 in nude rat), colon (HCT-116, HT-29), triple-negative breast (MDA-MB-231), prostate (PC-3), pancreatic (BxPC3), and Ewing's sarcoma. (**B**) Rodent tumor models: bladder (mouse SV40), breast (mouse 4T1), pancreatic (c-myc transgenic mouse), and brain (rat CNS-1).

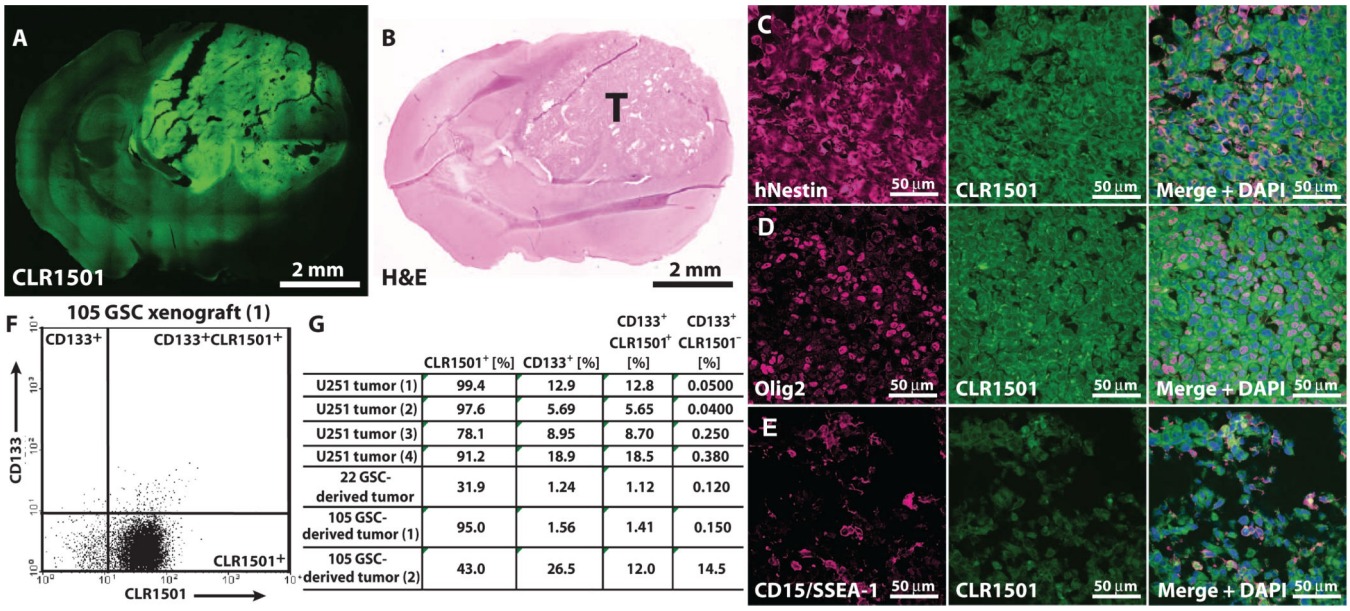

	CLR1501$^+$ [%]	CD133$^+$ [%]	CD133$^+$ CLR1501$^+$ [%]	CD133$^+$ CLR1501$^-$ [%]
U251 tumor (1)	99.4	12.9	12.8	0.0500
U251 tumor (2)	97.6	5.69	5.65	0.0400
U251 tumor (3)	78.1	8.95	8.70	0.250
U251 tumor (4)	91.2	18.9	18.5	0.380
22 GSC-derived tumor	31.9	1.24	1.12	0.120
105 GSC-derived tumor (1)	95.0	1.56	1.41	0.150
105 GSC-derived tumor (2)	43.0	26.5	12.0	14.5

Fig. 5. CLR1501 labeling of GSCs in vivo

CLR1501 was administered to mice harboring GSC-derived orthotopic gliomas 4 days before sacrifice. (**A** and **B**) Confocal microscopy verified CLR1501 uptake in histologically confirmed tumor [A: CLR1501 = green; B: hematoxylin and eosin (H&E), T = tumor]. (**C** to **E**) Immunohistochemistry for stem cell markers, including human-specific nestin (hNestin) (C), Olig2 (D), and CD15/SSEA-1 (E). DAPI (4′,6-diamidino-2-phenylindole) (blue) is shown in merged images. (**F** and **G**) Ex vivo flow cytometry analysis with CD133 (105 GSC-derived tumor-1) to quantify CD133$^+$/CLR1501$^+$ colocalization in GSC-derived and U251 xenografts. The percentage of marker-positive cells in total number of tested tumor cells is listed in (G).

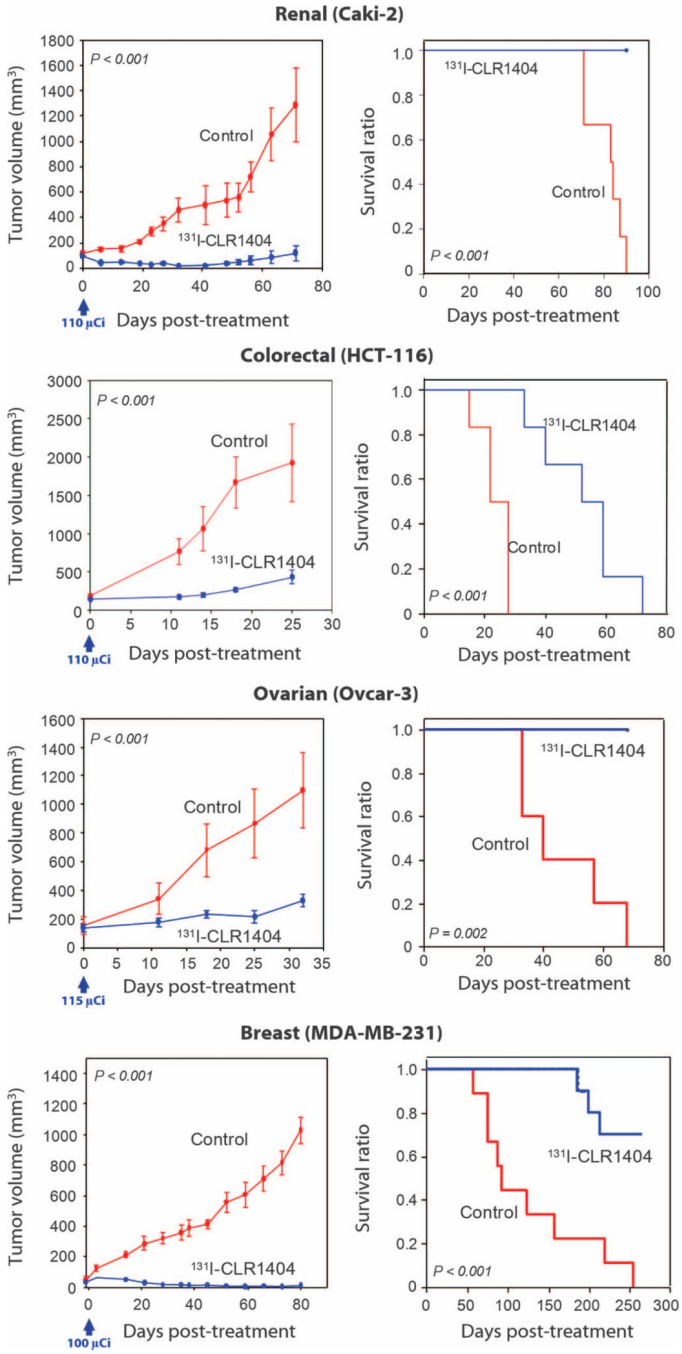

Fig. 6. Tumor growth and animal survival after ^{131}I-CLR1404 therapy

Nude mice harboring human tumor xenografts (n = 6 renal, 6 colorectal, 5 ovarian, and 9 breast) were administered a single ^{131}I-CLR1404 dose (arrow). Control animals were administered a mass-equivalent CLR1404 dose (n = 6). Data are mean tumor volumes ± SEM. P values for tumor growth curves determined by one-way repeated-measurement ANOVA. P values for survival curves were constructed by Kaplan-Meier method and analyzed via log-rank test.

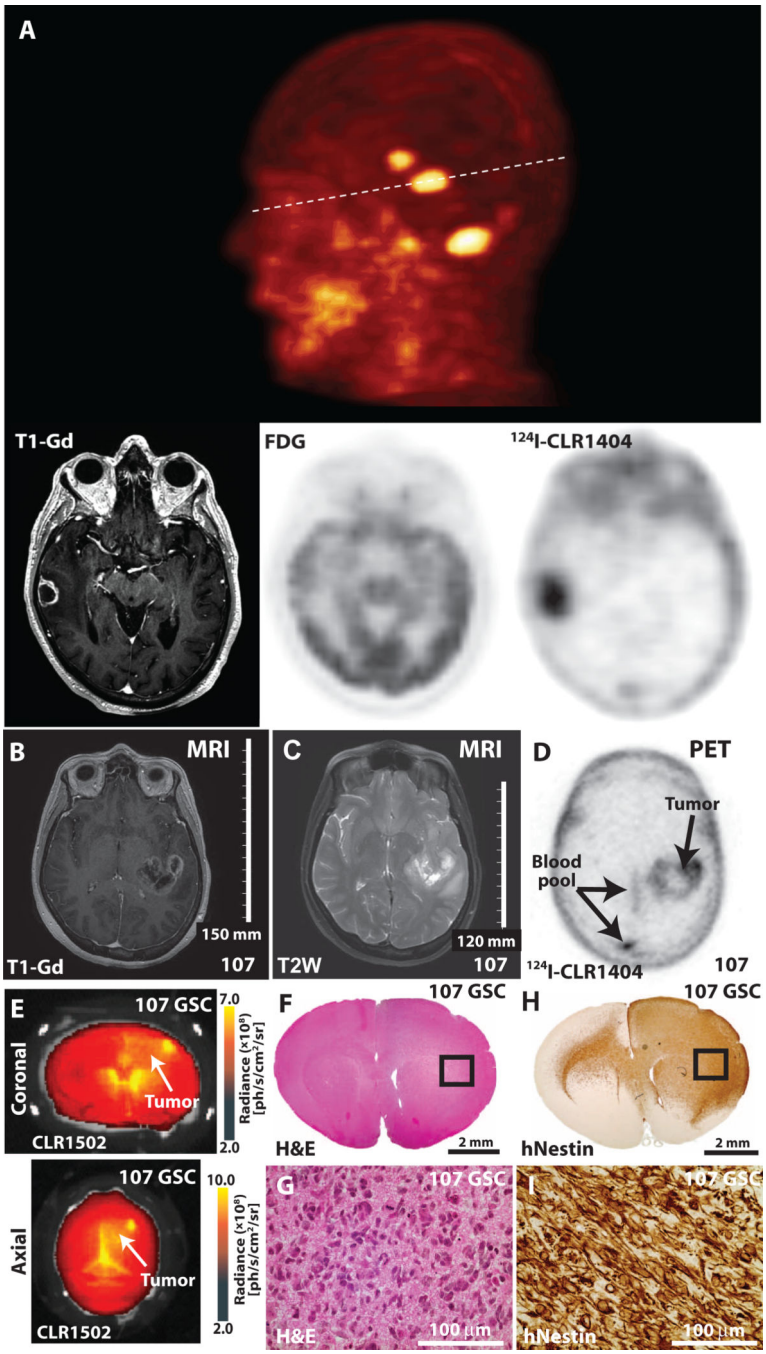

Fig. 7. Imaging of brain tumor patients and patient-derived xenografts

(**A**) Metastatic NSCLC patient. PET imaging 6 days after intravenous ^{124}I-CLR1404 administration revealed three previously unknown brain lesions suspicious for metastases (3D reconstruction). Lesions were verified via contrast-enhanced MRI [T1–gadolinium (Gd), arrow], but not detected on surveillance ^{18}F-FDG PET/CT, and present on ^{124}I-CLR1404 PET (dotted line = axial PET section). (**B** to **D**) Grade IV glioma patient. A patient diagnosed with suspected left insular GBM on T1-gadolinium–enhanced (B) and T2-weighted (C) MRI was confirmed on surgical pathology. Preoperative PET imaging

obtained 2 days after intravenous ^{124}I-CLR1404 administration revealed heterogeneous tumor uptake in a different pattern than T1-contrasted MRI, with low background signal in venous sinus blood pool (arrows) and normal brain (tumor/brain ratio = 28) (D). (**E** to **I**) Fluorescent CLR1502 imaging 4 days after administration showed uptake and localization in line 107 GSC-derived xenografts (E). Histological confirmation of line 107 GSC-derived xenografts: H&E (F and G) and human-specific nestin staining (brown in H and I).